AEROTHERMAL ANALYSIS OF REUSABLE LAUNCHER SYSTEMS DURING RETRO-PROPULSION REENTRY AND LANDING

Tobias Ecker[†], Franziska Zilker[†], Etienne Dumont[⋆], Sebastian Karl[†], and Klaus Hannemann[†]

[†] *German Aerospace Center (DLR), Institute for Aerodynamics and Flow Technology, Bunsenstr. 10, Göttingen, Germany, Email: tobias.ecker@dlr.de*

[⋆] *German Aerospace Center (DLR), Institute of Space Systems, Robert-Hooke Str. 7, Bremen, Germany*

ABSTRACT

The structural and thermal loads during first stage reentry may impact significantly the structural and thermal design and thus influence the payload performance and launch service cost of expendable launch vehicles. Many studies have focused on the effect of counterflowing jets emanating from blunt capsules on drag and aerothermal fluxes. However, for slender rocket shape bodies the database is still sparse. For this purpose CFD studies of the flow fields around a reusable first stage during reentry at freestream Mach numbers between 9.45 and 5.09 were carried out in close conjunction with the system analysis and trajectory design of potential future European carrier systems. The results of this study show that the integral heat uptake with hot retro-propulsion is generally higher than heat uptake at a ballistic state. However, the supersonic retro-propulsion maneuver redistributes the high heat loads from the baseplate area to the entire vehicle surface, therefore reducing local thermal loads.

KEYWORDS

retro-propulsion, launcher aerothermodynamics, counterflowing jet, exhaust plume

NOMENCLATURE

GTO	Geostationary Transfer Orbit
LES	Large Eddy Simulation
RANS	Reynolds Averaged Navier-Stokes
RTLS	Return To Launch Site
SRP	Supersonic retro-propulsion

1 INTRODUCTION

With the advent of the Falcon 9 successfully re-used first stage launch vehicle, there has been increased interest in the aerothermal aspects of supersonic retro-propulsion (SRP) and its consequences for vehicle design and pre-design. In particular, the structural and thermal loads occurring during reentry may impact specific details of the structural and thermal design and thus influence the payload performance and launch service cost of reusable launch vehicles. For this purpose several computational fluid dynamics (CFD) studies [1, 2] of the flow fields around the first stage during reentry were carried out in close conjunction with the system analysis and trajectory design aspects of a reusable first stage. In the current study we focus on the influence of plume-vehicle interaction, plume-plume interaction and plume chemistry effects on the thermal fluxes of a first stage launcher during retro-propulsion. Utilizing the resulting wall heat flux information, an aerothermal database is generated and used to determine the time-dependent wall temperature increase during the SRP. Additionally, the heat flux database modeling approach is validated against direct determination of wall heat flux from known temperature distributions. Further, the wall heat fluxes during the ballistic non-propulsive phase and the landing phase are investigated for selected trajectory points. In the course of this study the influence of engine conditions and gas models on the integral thermal loads are determined.

1.1 Previous studies

To date the research on supersonic retro-propulsion or more generally counterflowing jets in supersonic freestream has mainly concentrated on sphere-like and blunt compact bodies. The physics of counterflowing jets play an important role in these active reentry concepts and have been studied extensively. Daso et al. [3] gave an extensive overview on counterflowing jets in supersonic freestream with applications to capsule reentry. The idea is to modify the external flowfield of vehicles traveling at transonic to hypersonic speeds, in order to reduce wave drag, aerothermal loads or to decelerate the vehicle during reentry [4, 5,

3]. For thermal protection of the vehicle it is necessary that the secondary flow induced from the counterflowing jets creates a layer separating the vehicle from the main flow [4]. The thermal loads are then redistributed from the stagnation point in front of the vehicle to a reattachment/stagnation region further downstream.

In their paper, Daso et al. [3] presented an experimental study on a 2.6% scale Apollo capsule model using a single cold retro-jet at Mach 3.48 and 4.0 freestream conditions. Their study was conducted using heat flux instrumentation, Schlieren imaging and supplemented by numerical modeling. They confirmed the presence of a long and short jet penetration mode. For the long penetration mode the leading detached shock wave is diffused and replaced by a series of compression waves. The short penetration mode jet is characterized by a barrel shock, which encloses the jet in the transverse axis and terminates with a strong shock downstream of the bow shock in front of the vehicle. Fluid accelerated at the interaction between the terminal shock and the jet barrel shock can impinge on the vehicle surface (generally on the outer edge), creating spots with localized high heat fluxes [6]. The foundation work by Finley [4] attributed this effect mainly to the presence of unsteady flow with thin jet layers.

Studies using multiple nozzle configurations on a 70-deg sphere-cone forebody have been performed at NASA AMES by Berry et al. [7]. The study investigated single, triple and quad nozzle configurations in free-stream Mach numbers from 2.4 to 4.6 and a unit *Re* number of $1.5\text{x}10^6$ 1/m via Schlieren photographs and pressure instrumentation. In the study, Berry et al. found the shock stand off distance to generally increase with thrust coefficient. For multi nozzle configurations the interaction between the jets appear to reinforce fluctuations in the region between the jets, leading to oscillations of the bow shock in front of the vehicle. Further, the level of unsteadiness seem to increase with increasing Mach number and thrust level.

So far most studies on counterflowing jets for reentry or general high speed vehicles applications were concerned with cold gas jets exhausting into atmosphere. For many studies [4, 5, 3, 7] reduction in pressure drag, skin-friction drag and thermal loads are observed.

The successful reentry of SpaceX Falcon 9's first stage has increased interest in investigating the aerothermal challenges a slender rocket vehicle faces during propelled reentry. Previously Ecker et al. [2] have studied the thermal loads during the Falcon 9 supersonic reentry. For their study they compared steady RANS using the Spalart-Allmaras one-equation eddy viscosity model with unsteady computations using the same turbulence model operated in LES mode. Studies by NASA [8] demonstrate the general application of numerical tools to investigate the supersonic retro-propulsion (SRP) flowfield of the Falcon 9, but no quantitative data is shown. For one of the first Falcon 9 re-entries, NASA tracked the first stage on its trajectory using two planes equipped with infrared cameras. The results of this challenging experiment were presented by Horvath et al. [9]. The surface temperature of the first stage during retro-propulsion estimated from infrared imaging was in general good agreement with previous surface based temperature measurements. The study found the peak absolute temperature to be below 450 K during the time the imagery was recorded. This is consistent with the previous estimates [2] of the sidewall surface temperature to be at approximately 400 K after retro-propulsion.

1.2 Trajectory

For the computations performed here we consider the two stage to orbit H565H130 launch vehicle [1] running on LOx and LH2. This configuration is designed to launch more than 7 tons to GTO with a first stage performing a RTLS. The development of the stage configuration and the trajectory considered in this study are discussed in detail in Dumont et al. [1]. The presented configuration and SpaceX Falcon 9 are similar concerning the overall launch profile. However, the reentry trajectory of this study's configuration and the the reentry trajectory of the Falcon 9 mission considered in reference [2] differ in altitude and conditions at which the reentry burn is initiated. The Dumont first stage has a significantly lower peak altitude (130 km) than Falcon 9 (200 km) and starts the reentry retro-propulsion maneuver at around 70 km compared to the 50 km of Falcon 9. For retro-propulsion maneuvers the engines are active for around 30 s. In the current reentry maneuver the first stage decelerates from M = 9.45 to 5.09. The trajectory is modeled as seven discrete points, at which steady state was assumed. The corresponding atmospheric conditions are listed in table 1. Point 8 refers to the retro-boost at landing and is therefore not part of the supersonic retro-propulsion trajectory.

2 METHODS

In this section the methodology, domain geometry and boundary conditions of the numerical analysis based on computational fluid dynamics (CFD) computations is detailed. Furthermore, the engine model, based on the performance data which was estimated in [1] and used for the trajectory analysis, is described.

2.1 Numerical model

All numerical investigations in the framework of the present study were performed with the hybrid structured/unstructured DLR-Navier-Stokes solver TAU [10], which is validated for a wide range of steady

Traj. point	t [s]	h [km]	M	$Re \times 10^5$	p_∞ [Pa]	T_∞ [K]	ρ_∞ [kg/m^3]
1 (Start SRP)	243	68.0	9.45	0.212	6.32	223.05	$9.87 \cdot 10^{-5}$
2	247	63.3	8.73	0.361	12.7	236.21	$1.88 \cdot 10^{-4}$
3	252	58.5	8.0	0.595	25	249.65	$3.49 \cdot 10^{-4}$
4	257	53.6	7.27	0.952	48	263.37	$6.35 \cdot 10^{-4}$
5	263	48.3	6.54	1.604	94.1	270.65	$1.21 \cdot 10^{-3}$
6	271	42.1	5.82	3.456	209	256.93	$2.84 \cdot 10^{-3}$
7 (End SRP)	278	36.9	5.09	6.461	426	242.37	$6.13 \cdot 10^{-3}$
8 (Landing)	368	$5.1 \cdot 10^{-3}$	$1{\cdot}10^{-4}$	0	$1.01 \cdot 10^5$	288.15	1.22

Table 1: Freestream boundary conditions at retro-propulsion trajectory points.

and unsteady sub-, trans- and hypersonic flow cases. The TAU code is a second order finite-volume solver for the Euler and Navier-Stokes equations in the integral form using eddy-viscosity (RANS), Reynolds-stress or detached- and large eddy simulation (LES) for turbulence modeling. The AUSMDV flux vector splitting scheme was applied together with MUSCL gradient reconstruction to achieve second order spatial accuracy.

The applied models for thermodynamic and transport properties [11] are based on a non-reacting mixture of two thermally perfect gases (air and engine exhaust gas) along the entire supersonic retro-propulsion trajectory, as well as a finite rate chemistry model for the exhaust gas for a selected case.

2.2 Geometry and boundary conditions

The simplified vehicle geometry, which features a length of 57.2 m and a diameter of 6.4 m, is represented by a generic cylinder with a symmetrical nine engine configuration at the base. SpaceX calls this octagonal distribution around one center engine the *octaweb* configuration. During the supersonic reentry maneuver only three of the nine engines are used. For the purpose of the presented studies the nozzle outflow conditions are imposed onto the active engines as a Dirichlet boundary condition. The basic stage shape, engine configuration and nomenclature is shown in figure 1.

2.3 Engine model

The engine exhaust flow was modeled as an 2D axisymmetric converging-diverging contoured nozzle flow (figure 2a). The nozzle is 2.3 m long and has an exit diameter of 1.3 m. Several engine conditions were investigated (cf. table 2). The exhaust gas composition at the throat was estimated using CANTERA [12] for the given engine pressure and an O/F of 6.84 and then modeled as a thermally perfect and frozen gas. The exhaust gas composition can be found in reference [1]. The plenum temperature was then varied to set the engine mass flow rate to be close to the real

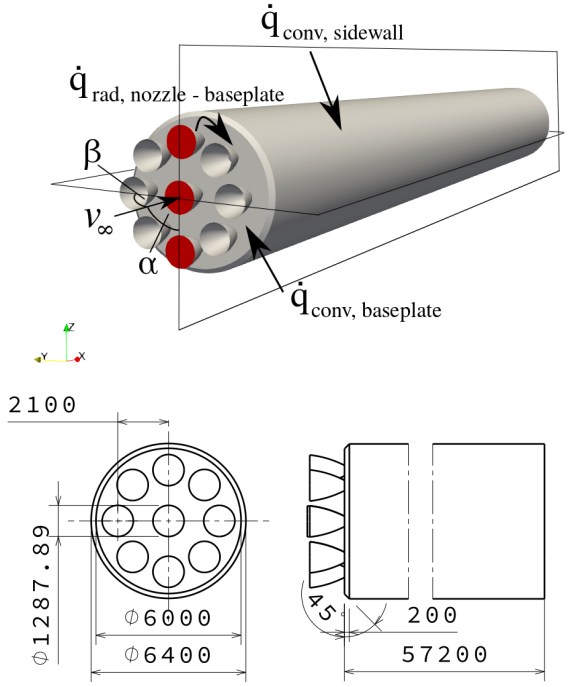

Figure 1: Vehicle geometry, considered heat fluxes and flow angles during the SRP maneuver.

engine values (condition **A**). The **B**aseline configuration uses the plenum temperature obtained from the original chemical equilibrium calculation. All chemical and non-equilibrium effects present while expanding the flow through the nozzle are ignored for engine configurations A and B. For one additional case, where the plume chemistry was considered, the nozzle flow was modeled as a chemical equilibrium flow (condition **C**). If not specifically mentioned all results shown are for the **B**aseline engine configuration.

The following boundary conditions were used:

- Nozzle inlet flow set to the combustion chamber conditions (p and ρ (cf. table 2))
- Nozzle wall as viscous and isothermal at 1000 K
- Nozzle outflow, i.e. exit plane, to 0.7 bar (ideal expansion)

Config.	p_t [bar]	T_t [K]	ρ_t [kg/m^3]	chemistry
A(dapted)	120	3900	5.5	frozen
B(aseline)	120	3700	5.9	frozen
C(hemical)	120	3700	5.5	chem. eq.

Table 2: Engine parameters.

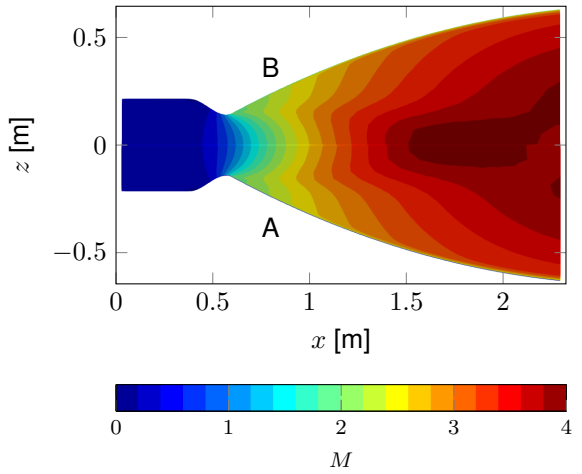

(a) Mach number; B top, A bottom.

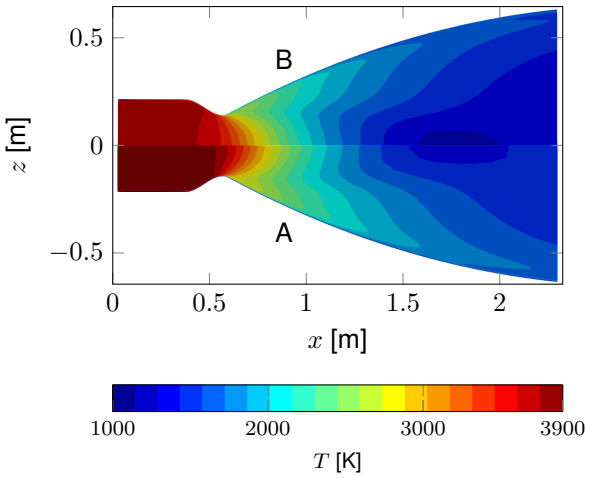

(b) Flow temperature; B top, A bottom.

Figure 2: Nozzle flow

2.4 Finite rate chemistry model

The chemical kinetic mechanism used for studying some of the plume chemistry effects was first presented by Jachimowski [13]. Jachimowski developed this model for the combustion of hydrogen and demonstrated its application for supersonic combustion in a scramjet. The behavior of the mechanism was optimized through comparison with data obtained from shock-tube and flame studies. For a representative scramjet combustor conditions he found the chemical kinetic effects to have significant influence on the prediction of the scramjet internal thrust. At high Mach numbers the recombination reactions appear to control the combustion process.

The 9 species and 19 reactions mechanism was updated based on more current literature values and the nitrogen three body efficiencies by Gerlinger et al. [14]. The mechanism and the reaction rate coefficients used in this study are given in table 3.

2.5 Coupling between CFD and structural heating

A simple lumped mass model is used to estimate the wall temperature during the retro-propulsion maneuver. For this purpose the casing is modeled as a number of thin aluminum rings, for each of which a 0 D heat equation is solved using a Euler scheme. The coupling between the aerothermal database and the integration algorithm is shown in figure 3.

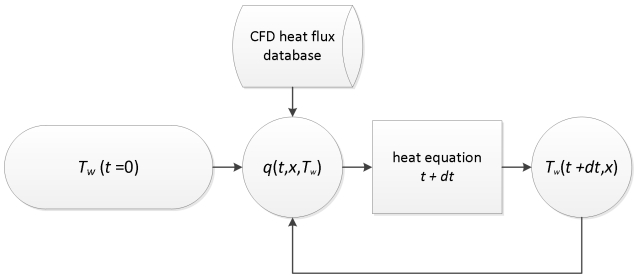

Figure 3: Aerothermal database structural heating coupling

The database contains the CFD simulation outputs of the convective wall heat fluxes $\dot{q}_\mathrm{w}$ as a function of the wall temperature at each surface element grid node. Since the lumped mass model is assumed, each grid node represents a surface element, in which the applied heat flux is distributed instantly and homogeneously. The resulting temperature rise is calculated from the following energy balance equation [2]:

$$T_\mathrm{w}(t+dt,\,\vec{x}) = T_\mathrm{w}(t,\,\vec{x}) + \frac{\dot{q}_\mathrm{w}(t,\,\vec{x},\,T_\mathrm{w}(t,\,\vec{x})) + \dot{q}_{rad}(t,\,\vec{x})}{\rho\, b\, c_p}\, dt \quad (1)$$

The wall element at position $\vec{x}$ and temperature $T_w(t,\,\vec{x})$ is exposed to the wall heat flux $\dot{q}_\mathrm{w}(t,\,\vec{x},T_\mathrm{w}(t,\,\vec{x}))$ over the time dt and heats up to the temperature $T_w(t{+}dt,\,\vec{x})$. ρ, b and c_p stand for the density, thickness, and specific heat capacity at constant pressure of the wall material aluminum (cf. table 4 and figure 8a for the thickness distribution of the sidewall).

$$\dot{q}_{rad}(t,\,\vec{x}) = \sigma\epsilon\left(T_\infty^4 - T_\mathrm{w}(t,\,\vec{x})^4\right) \quad (2)$$

The radiation heat transfer is modeled as simple grey body radiation, where σ is the Stefan-Boltzmann constant and ϵ the emissivity coefficient of the object.

Table 3: Jachimowski [13, 14] reaction mechanism. Units in m, mol, J, s.

No.	Reaction	Rate Constants A	n	E
1	$H_2 + O_2 \rightleftharpoons HO_2 + H$	1.0000e+08	0.00	2.3430e+05
2	$H + O_2 \rightleftharpoons OH + O$	2.6000e+08	0.00	7.0291e+04
3	$O + H_2 \rightleftharpoons OH + H$	1.8000e+04	1.00	3.7238e+04
4	$OH + H_2 \rightleftharpoons H_2O + H$	2.2000e+07	0.00	2.1548e+04
5	$2\,OH \rightleftharpoons H_2O + O$	6.3000e+06	0.00	4.5606e+03
6[a]	$H + OH + M \rightleftharpoons H_2O + M$	2.2000e+10	-2.00	0.0000e+00
7[b]	$2\,H + M \rightleftharpoons H_2 + M$	6.4000e+05	-1.00	0.0000e+00
8[c]	$H + O + M \rightleftharpoons OH + M$	6.0000e+04	-0.60	0.0000e+00
9[d]	$H + O_2 + M \rightleftharpoons HO_2 + M$	2.1000e+03	0.00	-4.1840e+03
10	$HO_2 + H \rightleftharpoons 2\,OH$	1.4000e+08	0.00	4.5187e+03
11	$HO_2 + H \rightleftharpoons H_2O + O$	1.0000e+07	0.00	4.5187e+03
12	$HO_2 + O \rightleftharpoons O_2 + OH$	1.5000e+07	0.00	3.9748e+03
13	$HO_2 + OH \rightleftharpoons H_2O + O_2$	8.0000e+06	0.00	0.0000e+00
14	$2\,HO_2 \rightleftharpoons H_2O_2 + O_2$	2.0000e+06	0.00	0.0000e+00
15	$H + H_2O_2 \rightleftharpoons H_2 + HO_2$	1.4000e+06	0.00	1.5062e+04
16	$O + H_2O_2 \rightleftharpoons OH + HO_2$	1.4000e+07	0.00	2.6778e+04
17	$OH + H_2O_2 \rightleftharpoons H_2O + HO_2$	6.1000e+06	0.00	5.9831e+03
18[e]	$H_2O_2 + M \rightleftharpoons 2\,OH + M$	1.2000e+11	0.00	1.9037e+05
19	$2\,O + M \rightleftharpoons O_2 + M$	6.0000e+01	0.00	-7.5312e+03

[a] $H_2O = 6.0$
[b] $H_2 = 2.0$, $H_2O = 6.0$
[c] $H_2O = 5.0$
[d] $H_2 = 2.0$, $H_2O = 16.0$
[e] $H_2O = 15.0$

3 SUPERSONIC RETRO-PROPULSION

All numerical investigations for the aerothermal analysis of the first stage launcher during descent were performed using the Spalart-Allmaras one-equation eddy viscosity model [15]. The applied model for thermodynamic and transport properties are based on a non-reacting mixture of thermally perfect gases (air and engine exhaust) and are derived from the CEA [11] thermodynamic and transport databases.

3.1 Plume-vehicle interaction

The flowfield structure present in supersonic retro-propulsion of a slender body is similar to the flowfield encountered by blunt capsules with retro-propulsion. The flowfield for one trajectory point is shown in figure 5. Similar to the flowfield described by Daso et al. [3], the SRP flowfield is characterized by a barrel shock, which encloses the jet in the transverse axis and then terminates with a strong shock downstream of the bow shock in front of the vehicle. For the case of a slender rocket body the ratio between jet exit diameter and vehicle diameter, but also the thrust coefficient is much higher than ordinarily applied to reentry capsules. This leads to a very large shock stand off distance (most similar to large thrust coefficient cases as shown by [7]) and a wide distribution of reattachment locations.

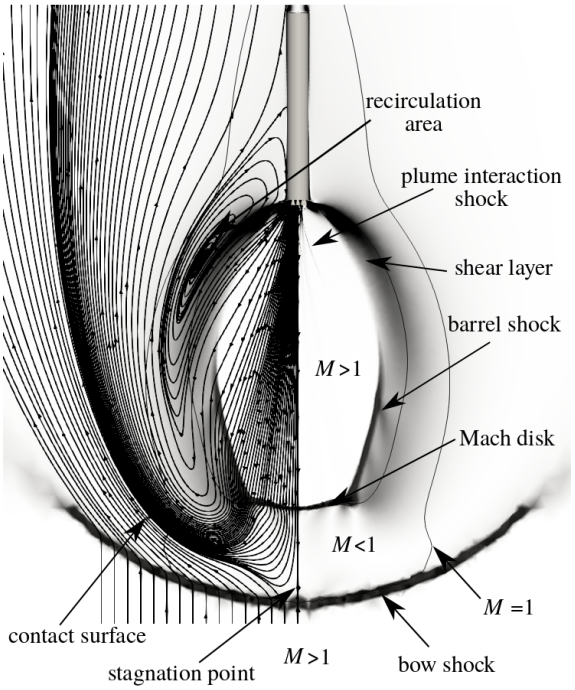

Figure 4: Supersonic retro-propulsion flowfield at trajectory point 1.

The development of the plume along the retro-propulsion trajectory is shown in figure 5 and strongly

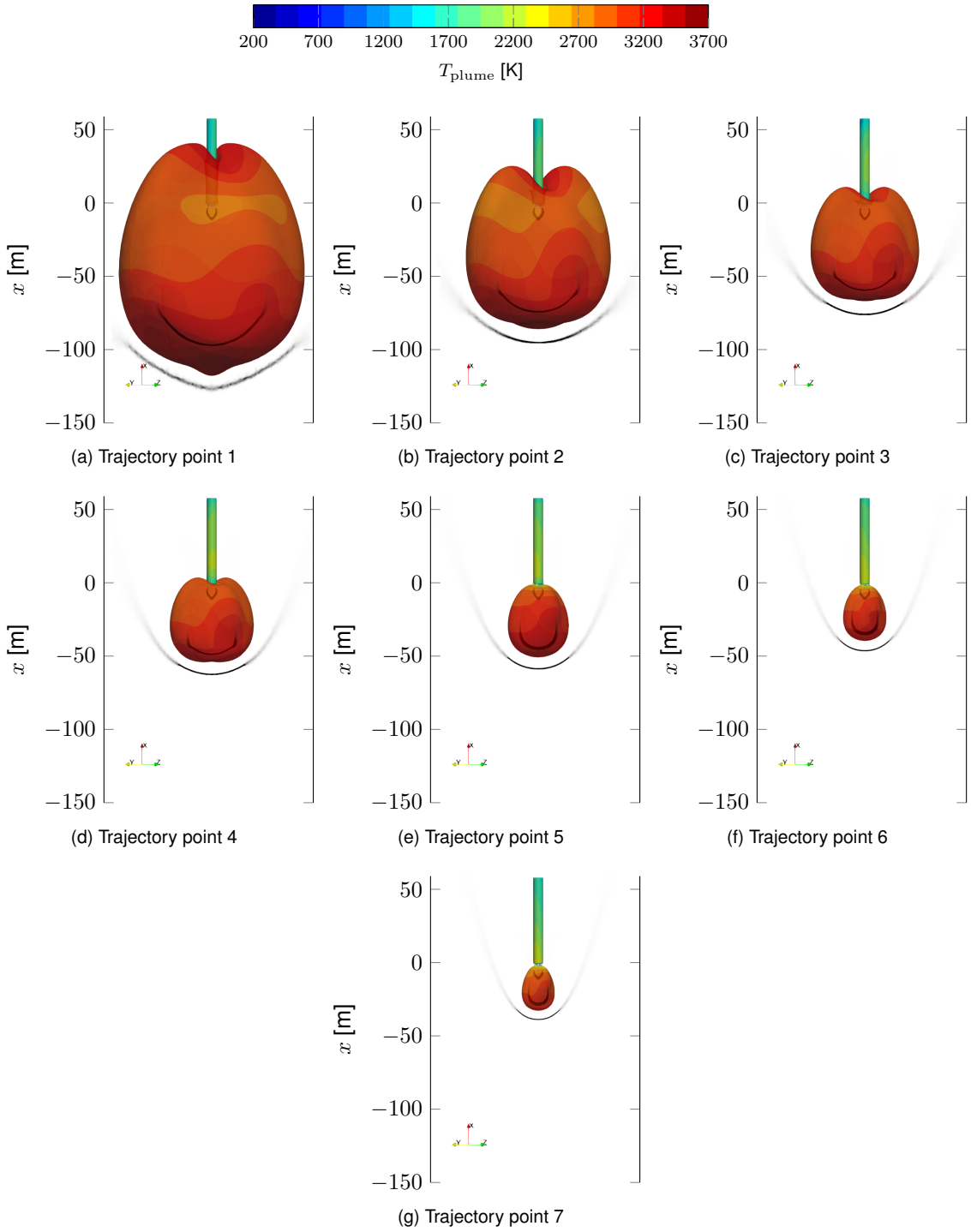

Figure 5: Evolution of supersonic retro-propulsion plume flow along the trajectory for exhaust mass fraction $w_{\text{exhaust}} = 0.6$. Active engines along z axis (green). Engine configuration B.

depends on the engine pressure ratio. At high altitudes the plume boundary reaches a significant extension and the entire vehicle is submerged in hot exhaust gases. With increasing pressure the plume slowly retracts towards the base and the plume vehicle interface ceases. Over the course of the trajectory, the plume size reduces significantly from about 100 m to several 10 m, allowing the shocks to move closer to the vehicle. The gas temperature near the vehicles sidewall increases with decreasing altitude. The area of highest surface gas temperature moves to the aft of the vehicle and changes in lateral position. The location of the highest temperatures moves from parallel to the active engines (z axis) at the beginning of the SRP maneuver to perpendicular to the active engines (y axis) at the end of the SRP maneuver.

3.2 Plume-plume interaction

Due to the in-line configuration of the three engines active during reentry, the plume envelopes the vehicle asymmetrically. The plume at trajectory point 1 is chosen as an example in figure 6, but the plume asymmetry is present at other trajectory points as well.

The reason for this particular shape lies in the interaction between the three plumes. They form oblique shocks on impingement as shown in gray scale in figure 6 (right). At the beginning of the SRP maneuver, when the atmosphere pressure is low, the plume expands past the shocks and accelerates up to M = 12 6 (left).

3.3 Plume chemistry effects

For the last trajectory point with the lowest freestream Mach number the Jachimowski [13] finite rate chemistry model was applied. The resulting flowfield compared to the engine configuration A flowfield is displayed in figure 7. Several differences can be found: The first difference is the slightly higher exhaust gas temperature due to the chemical effects in the diverging section of the exhaust nozzle. Another main difference is due to the dissociation and recombination reaction pathways, which lead to a significant lower temperature after the bow shock and very high levels of Hydroxide (OH) in this region. The OH mass fractions are highest right after the bow shock and are present within the outer shear layer of the plume. While this OH layer recombines further upstream along the plume interface, leading to an temperature increase, generally lower gas temperatures are present when compared to the engine configuration A or B case. In opposite to the main flow temperature development, generally higher gas temperatures (A: 1400 K, C: 2250 K) are present in the vicinity of the baseplate and nozzles. This is not explained from the higher exhaust temperatures alone but may be an effect of post combustion of excess Hydrogen within the plume-plume shear layer.

4 AEROTHERMAL EVOLUTION OF FIRST STAGE DURING SRP

The analysis of the aerothermal evolution of the first stage during SRP is built on a heat flux database based on the previously described trajectory points as well as supporting points close to nonlinear trends within the Mach and unity Reynolds number conditions studied. For more details on the database points refer to Dumont et al. [1]. The Mach and unity Reynolds number are used to describe the physical parameter space enabling interpolation using physical parameters instead of the time domain. For each database point CFD calculations at constant wall temperature of 300 K and 400 K were performed. The final aerothermal database consists of the linearly interpolated heat flux as a function of trajectory time and sidewall coordinate. This database is then coupled into a simple lumped mass structure model in order to estimate the wall temperature change along the trajectory.

4.1 Wall temperature evolution

In order to estimate the wall temperature distribution during SRP the heat equation presented in section 2.5 is integrated along the trajectory. The wall thickness distribution for this configuration is indicated in figure 8a. These values do not take into account stiffening elements or insulation covering the tanks, but rather represent the minimum thickness of the structure. Further no conduction between elements, as well as heat transfer to the vehicle inside is considered for the results presented. Radiation was neglected due to the relatively low wall temperatures.

Property	
c_p [J/kg K]	864
ρ [kg/m^3]	2840
$b_{sidewall}$ [mm]	1.8 - 3.4
$b_{baseplate}$ [mm]	5.0

Table 4: Aluminum properties for baseplate and sidewall material [1].

The evolution of the sidewall temperature for the SRP trajectory is illustrated in figure 8. At the beginning of the reentry burn, the wall temperature is assumed to be at uniform 300 K. The wall thickness distribution leads to generally higher temperatures at the LH2 tank, due to its low wall thickness. The plume vehicle interaction during reentry leads to almost 100 K temperature increase at this location. Note that the maximum temperature coincides with the plume impingement location.

4.2 Passive reentry

Before the three engines are ignited at trajectory point 1, the first stage is flying with M = 9.45 at an altitude of h = 68 km. The bow shock forms directly in front of the nozzle, heating the freestream up to 3400 K, due to the high Mach number. Thus, the aft of the first stage sees most of the hot gas from the bow shock (figure 9a), particularly the sidewall area immediately after the edge. After the retro-propulsion maneuver, the first stage is decelerated to M = 5.09 at h = 36.9 km and the heating of the freestream over the shock is significantly reduced to 1400 K. Therefore, the gas temperature surrounding the first stage is also considerably lower (cf. figure 9b).

It is clearly visible that the aft of the first stage is highly affected by shock and stagnation point heat-

ing of the flow. The wall heat fluxes at the aft are up to eight times (respectively three times in figure 9d) higher when compared to the case with ignited engines at the same flow conditions. The heat flux from the hot plume to the sidewall mainly affects the upper part of the first stage, where it is up to two times higher compared to the case with deactivated engines.

4.3 Flow history influence on heat flux prediction

The presented database is based on uniform wall temperature (300 K and 400 K) distributions and does not take into account flow field changes due to the wall temperature evolution along the trajectory. In order to estimate the error due to this model simplification, the database is validated at trajectory points 2, 4 and 7. For these points the sidewall temperature profiles (see in figures 8c, 8e and 8h), obtained from the integral heating during the trajectory, are applied as prescribed wall temperature boundary conditions. The obtained wall heat fluxes are compared to the heat fluxes from the database at the corresponding trajectory point.

At the beginning of the retro-propulsion maneuver (trajectory point 2) the database locally over-predicts the heat flux to the side wall by up to 35 %. Especially, the heat flux to the upper part on the active engine side, where the plume is impinging is overestimated. It would be expected, that the difference between simulation and database would be small at this trajectory point, since it is not far away from the initial temperature distribution. This deviation is believed to originate from a locally not fully steady solution. At trajectory point 4 the database under-predicts the heat flux by up to 20 %. A deviation between simulation and database heat flux at this point is expected since the wall temperature distribution differs significantly from the two temperature boundary conditions considered in the database. Trajectory point 7 shows little deviation between the simulation and the database (2 to 5 %). The relative root mean square error between simulation and database heatflux $(\dot{q}_{\mathrm{w,sim}} - \dot{q}_{\mathrm{w,db}})/\dot{q}_{\mathrm{w,sim}}$ is summarized in table 5. The largest error appears at trajectory point 2 due to the locally unsteady flow fea-

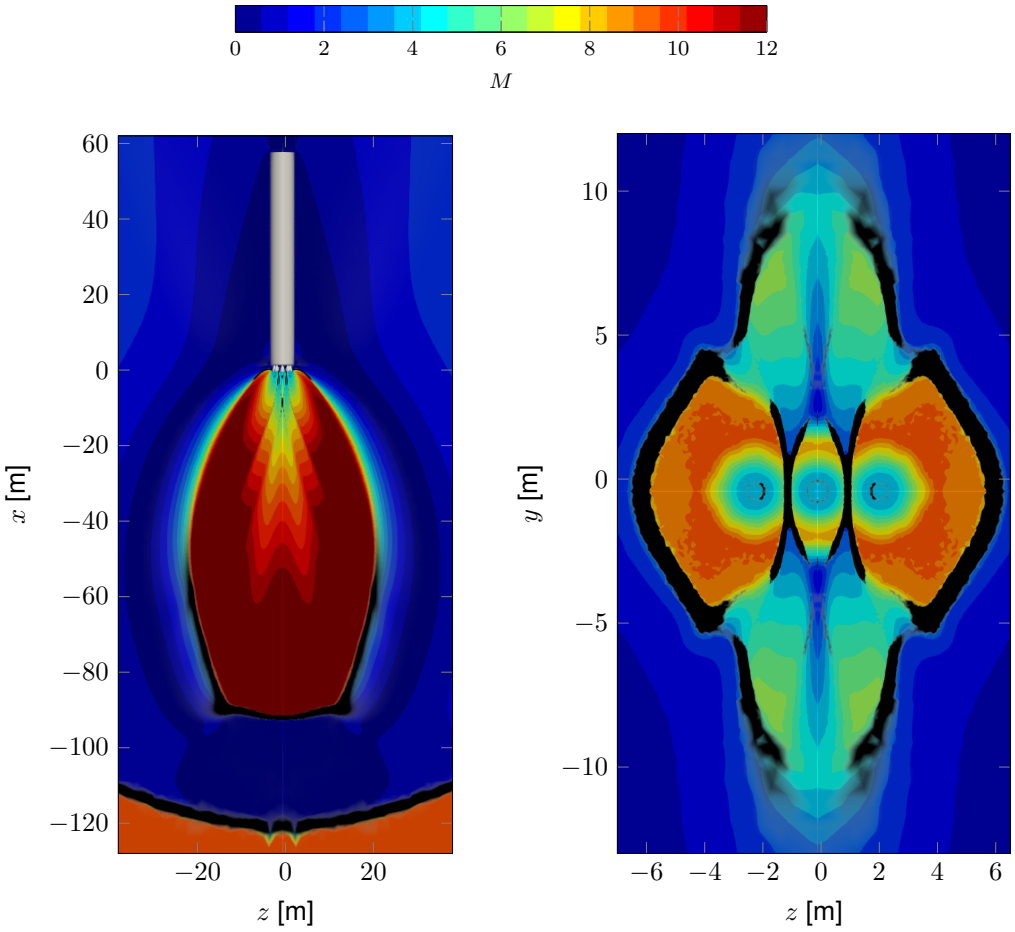

(a) M contours with shocks in gray scale.

(b) Plume interactions shocks and M contours 0.5 m downstream of nozzle exit at trajectory point 1.

Figure 6: Mach number distribution of plume-plume interaction at trajectory point 1 ($T_{\mathrm{w}} = 300$, $h = 68$ km, $M = 9.45$) with cut plane through plume 2 m downstream of the baseplate. Shocks indicated in grey scale. Engine configuration B.

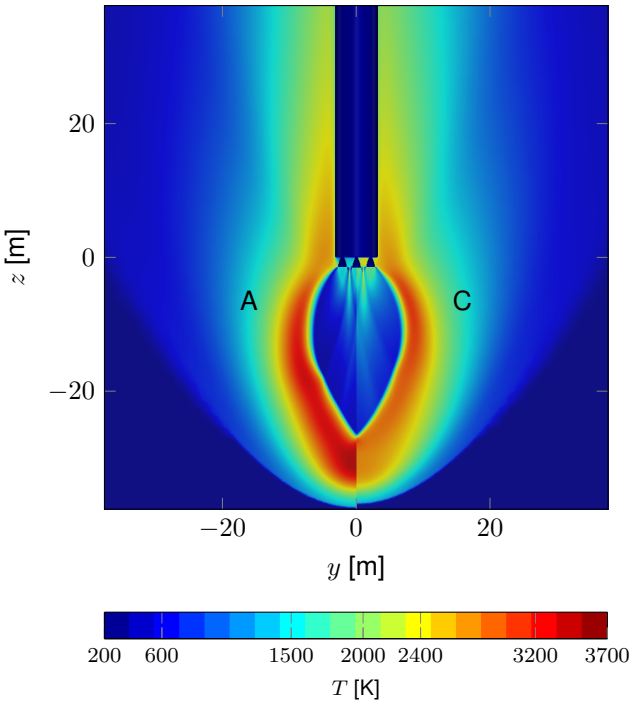

Figure 7: Reentry flowfield at trajectory point 7, engine condition A (left), engine condition C with combustion model applied (right).

tures and the lowest at point 7 where the simulation and database coincide. A previous study by Ecker et al. [2] estimated the error of the interpolated data to be within 3.2 % and 10 %. Within the current study the influence of flow history effects were estimated. For the cases considered these effects introduce uncertainties between 3 % and 17 % - however mainly induced due to areas with not fully steady state flow and less resultant from to wall temperature induced flow structure changes. These effects are local to some trajectory points, their influence on the final integral temperature profile is estimated to be less pronounced.

	RMS [%]
Trajectory point 2	17
Trajectory point 4	8
Trajectory point 7	3

Table 5: Relative root mean square error of $(\dot{q}_{\mathrm{w,sim}} - \dot{q}_{\mathrm{w,db}})/\dot{q}_{\mathrm{w,sim}}$ *in [%].*

4.4 SRP Integral loads

In order to compare the different engine configurations the overall heat flow rate to the sidewall and baseplate are integrated over the vehicle area. A comparison of the different configurations, as well as the passive reentry cases is shown in figure 10.

The maximum rate of heat flow reaches 18.5 MW, suggesting that the sidewall heat flow is predominant compared to the baseplate ($\dot{Q}_{\mathrm{max,b}} = 210$ kW). The overall heat flow rate to the first stage with deactivated engines is considerably smaller, not even half the heat flow rate with active engines (2.3 MW in the beginning and 7.5 MW at the end). For the engine configuration **A** the integral heat flow is slightly higher which was expected due to the higher plenum temperature. The heat flow for the case **C**, which includes combustion effects shows about 20% higher thermal loads - this is surprising as dissociation effects reduce the temperature behind the bow shock. For all three configurations the baseplate heat flow contribution is only marginal. For the baseplate a wall thickness of 5 mm was assumed. The effect of radiative cooling is relative low due to the low sidewall and baseplate temperatures.

The integral heating of the wall Q_{w} over the retropropulsion trajectory is given in table 6. The adapted engine configuration shows an about 14% higher integral heat load.

Engine config.	**A**	**B**
Q_{w} Sidewall	418.1 MJ	365.0 MJ
Q_{w} Baseplate	8.2 MJ	7.2 MJ
Q_{w} Total	426.3 MJ	372.2 MJ

Table 6: Integral heating Q_{w} *over the SRP trajectory (excl. radiation).*

5 VEHICLE GROUND INTERACTION

The landing boost was modeled as steady state during landing. The simulation was conducted with the central engine ignited, instants before the engine is switched off with an uniform surface temperature of 400 K. Landing legs where not considered, but the distance between nozzle exit and ground was set to 5 m as if landing legs were attached, holding the first stage in place. The freestream boundary condition is set to sea-level static, cf. table 1. The plume interacting with the ground is depicted in figure 11. The flowfield shows an over-expanded impinging wall jet, with oblique, coalescing shock waves forming at the nozzle lip and a tail shock on impinging. The central part of the plume reaches up to 3000 K on impinging. The plume continues to mix and extend up to 30 m circular around the first stage ($w_{\mathrm{exhaust}} = 0.05$) still having a temperature of approximately 700 K.

The first stage's sidewall is mildly affected by the hot plume: The lower part is exposed to near wall gas temperature of around 500 K leading to wall heat fluxes of maximum 10 kW/m^2 (figure 12a), whereas the baseplate is highly affected by the backflow of plume gases exiting the nozzle (figure 12b). Particularly, the area around the center nozzle sees the highest heat flux of 200 kW/m^2. The heat flux distribution suggests that part of the plume exiting from the nozzle reverses and impinges on the baseplate. After impingement, the hot gas flows out radially between the

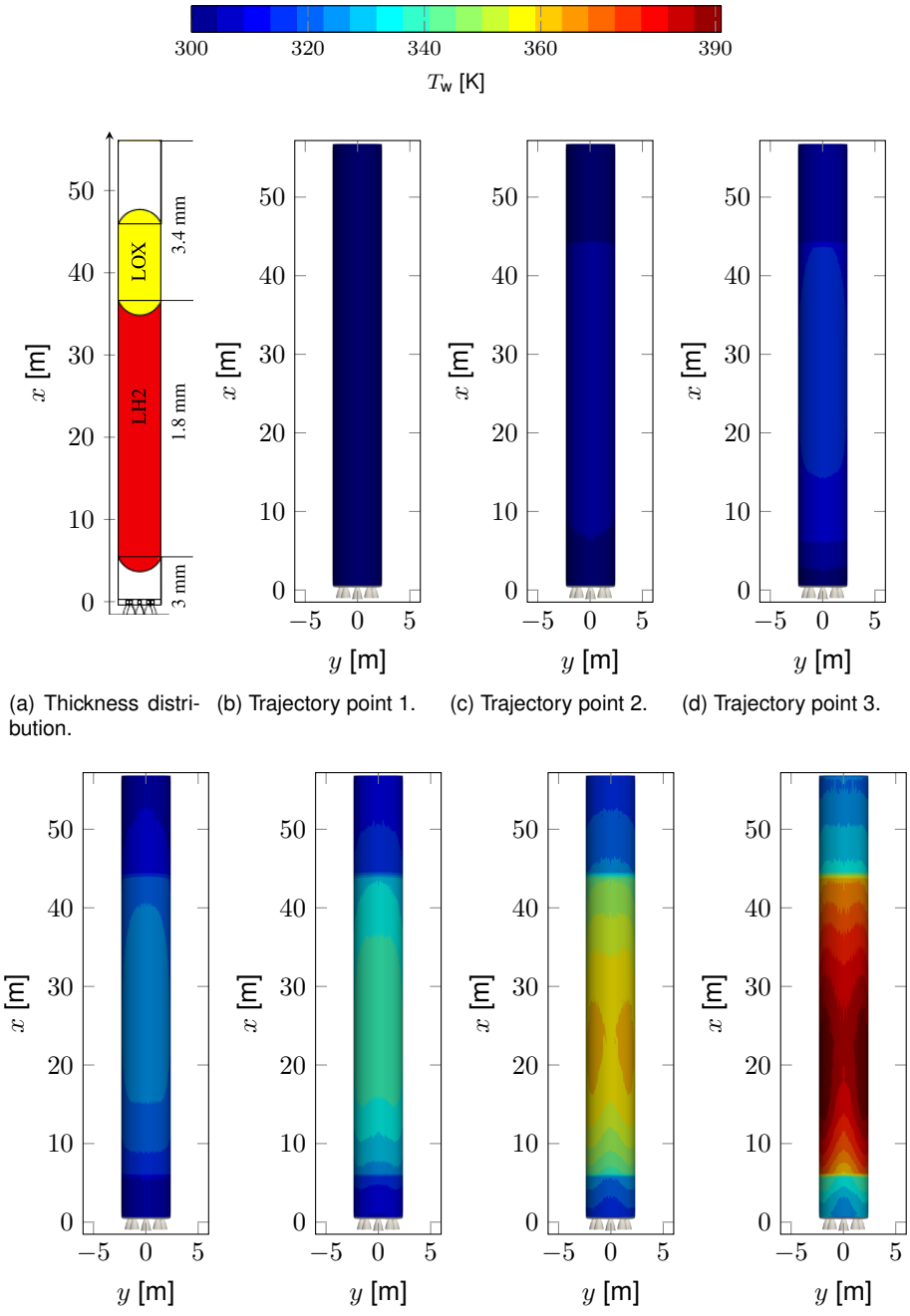

(a) Thickness distribution. (b) Trajectory point 1. (c) Trajectory point 2. (d) Trajectory point 3.

(e) Trajectory point 4. (f) Trajectory point 5. (g) Trajectory point 6. (h) Trajectory point 7.

Figure 8: Sidewall temperature evolution along SRP trajectory, active engines along z (normal to viewing plane). Engine configuration B.

nozzles, leading to a second zone of increased heat flux in the wake region of the outer nozzles. Radiation from the launch pad to the vehicle is not taken into account as it is highly dependent on the launch site structure.

6 CONCLUSIONS

This study shows that the thermal loads on the first stage's wall are strongly dependent on the supersonic retro-propulsion flowfield. The flowfield is characterized by a highly under-expanded plume flow exhausting into an opposing supersonic freestream. The sidewall loads are mainly affected by the interaction of the hot exhaust plumes with the oncoming freestream. The opposing freestream forces the plume flow to turn, immersing the whole first stage in hot exhaust gases. In the regions on plume reattachment the thermal loads are found to be the highest. With decreasing altitude the maximum thermal loads increase and move to the aft of the first stage, as the plume con-

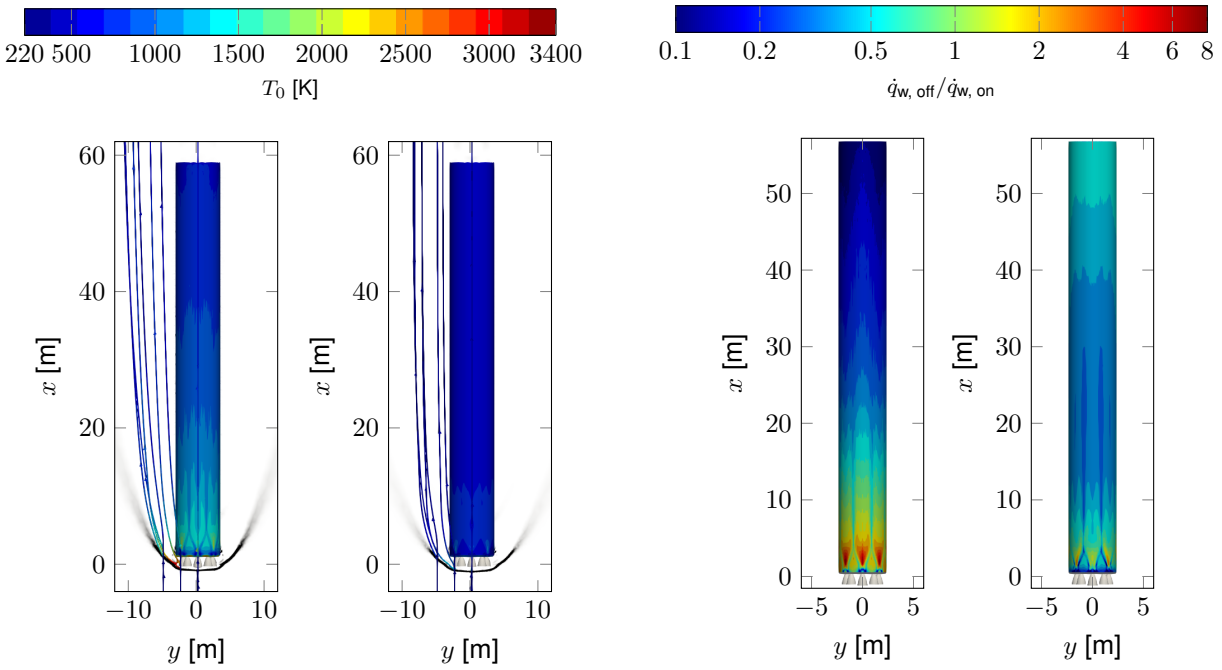

(a) Trajectory point 1 (b) Trajectory point 7.

Flowfield of first stage before and after retro-propulsion, streamlines and vehicle wall colored in T_0. Shock indicated via div$\vec{v}$ in gray scale.

(c) Trajectory point 1 (d) Trajectory point 7.

Heat flux ratio $\dot{q}_{\text{w, off}}/\dot{q}_{\text{w, on}}$ at sidewall before and after retro-propulsion.

Figure 9: Passive reentry before and after the SRP phase.

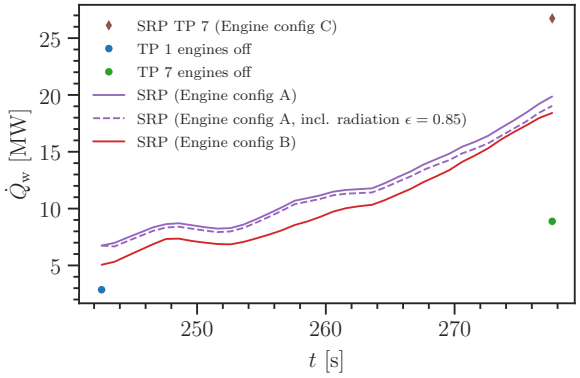

Figure 10: Rate of heat flow to sidewall and baseplate along trajectory for different engine configurations compared to ballistic reentry at the same conditions.

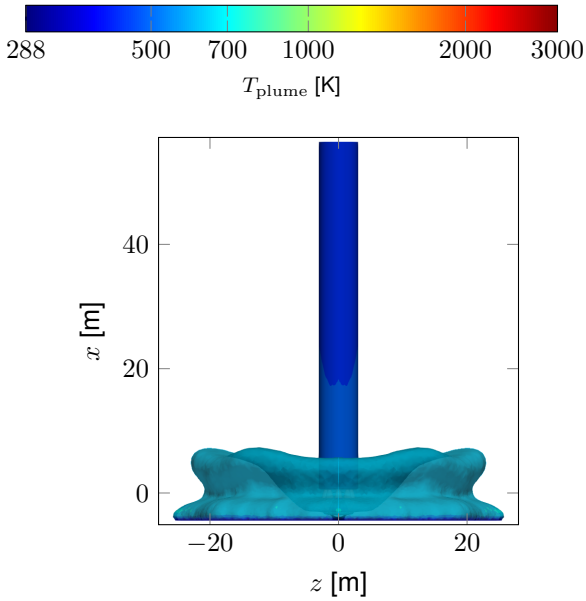

(a) Plume at $w_{\text{exhaust}} = 0.05$.

Figure 11: Plume temperature and extension during landing, only center engine active. Engine configuration B.

tracts due to the denser atmosphere. During the retro-propulsion trajectory the sidewall temperature rises by about 100 K to a maximum temperature of 400 K depending on the sidewall thickness distribution. Plume chemistry was taken into account for a single trajectory point using a Hydrogen/Oxygen combustion model. Dissociation and recombination effects within the vicinity of the plume lead to discernible temperature differences in the flowfield. Due the relatively low wall temperatures, cooling due to radiation dues not play a large role during the propulsive phase. The landing boost was modeled for a steady state during landing and shows relatively small heat loads on the sidewall but heat fluxes up to 200 kW/m^2 on the baseplate. The plume extends circular around the first stage reaching 60 m in diameter at 5 % mass fraction. The plume-air mixture has relatively high gas temper-

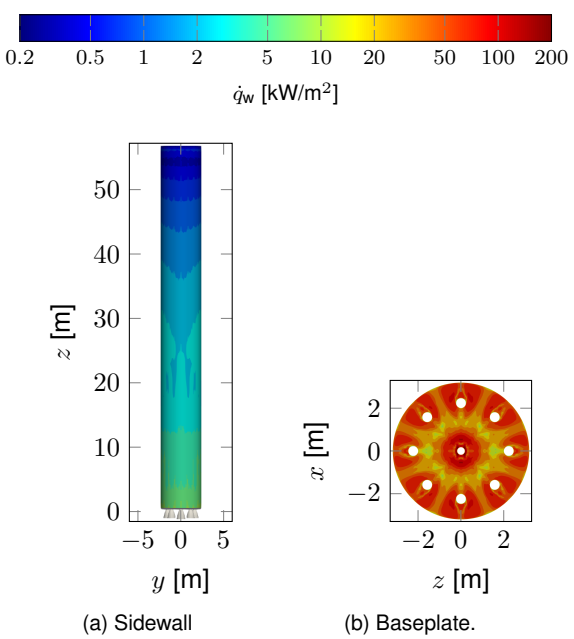

(a) Sidewall (b) Baseplate.

Figure 12: Wall heat fluxes at landing instants before engine shut down. Engine configuration B.

atures, which should be considered for the safety and operation conditions at the landing site.

In opposite to the classical approaches of heat flux reduction by creating a layer separating the vehicle from the main flow, integral heat uptake with hot retro-propulsion is generally higher than heat uptake at a ballistic state. However, the local distribution of heat flux is influenced strongly. With deactivated engines the heat loads are concentrated around the aft of the first stage and are increase by up to eight times. During the retro-propulsion maneuver the baseplate and aft are protected by the plume, which in turn causes 80 % higher thermal loads on the upper part of the sidewall. The integral heating of the first stage sidewall and baseplate over the retro-propulsion maneuver shows only a small contribution of the baseplate. This study shows that during the supersonic retro-propulsion maneuver the heat loads are redistributed from the baseplate area to the entire vehicle surface, therefore reducing local thermal loads.

REFERENCES

1. Dumont, E., Stappert, S., Ecker, T., et al. (2017). Evaluation of Future Ariane Reusable VTOL Booster stages. 68th International Astronautical Congress (IAC), Adelaide, Australia, 25-29 September 2017.
2. Ecker, T., Karl, S., Dumont, E., Stappert, S., and Krause, D. (2017). A Numerical Study on the Thermal Loads during a Supersonic Rocket Retro-propulsion Maneuver. AIAA Paper 2017-4878.
3. Daso, EO, Pritchett, VE, Wang, TS, Ota, DK, Blankson, IM, and Auslender, AH (2009). Dynamics of Shock Dispersion and Interactions in Supersonic Freestreams with Counterflowing Jets. AIAA Journal;47:1313–1326.
4. Finley, PJ (1966). The flow of a jet from a body opposing a supersonic free stream. Journal of Fluid Mechanics;26.
5. Meyer, B, Nelson, HF, and Riggins, DW (2001). Hypersonic Drag and Heat-Transfer Reduction Using a Forward-Facing Jet. Journal of Aircraft;38:680–686.
6. Warren, CHE (1960). An experimental investigation of the effect of ejecting a coolant gas at the nose of a bluff body. Journal of Fluid Mechanics;8.
7. Berry, SA, Rhode, MN, and Edquist, K (2014). Supersonic Retropropulsion Validation Experiment in the NASA Langley Unitary Plan Wind Tunnel. Journal of Spacecraft and Rockets;51:664–679.
8. K. Edquist, A. Korzun, K. Bibb, D. Schauerhamer and E. Ma, P. McCloud, G. Palmer and J. Monk (2017). Comparison of Navier-Stokes Flow Solvers to Falcon 9 Supersonic Retropropulsion Flight Data. AIAA paper 2017-5296.
9. Horvath, TJ, Aubuchon, VV, Rufer, S, et al. (2017). Advancing Supersonic Retro-Propulsion Technology Readiness: Infrared Observations of the SpaceX Falcon 9 First Stage. AIAA Paper 2017-5294.
10. Langer, S, Schwöppe, A, and Kroll, N (2014). The DLR Flow Solver TAU – Status and Recent Algorithmic Developments. AIAA Paper 2014-0080.
11. Gordon, S and McBride, BJ (1996). Computer Program for Calculation of Complex Chemical Equilibrium Compositions and Applications. Tech. rep. NASA Reference Publication 1311.
12. G. Goodwin, D, K. Moffat, H, and Speth, R (2015). Cantera: An Object-oriented Software Toolkit for Chemical Kinetics, Thermodynamics, and Transport Processes. Version 2.2.0. Tech. rep.
13. Jachimowski, CJ (1988). An analytical study of the hydrogen-air reaction mechanism with application to scramjet combustion [microform] / Casimir J. Jachimowski. National Aeronautics, Space Administration, Scientific, and Technical Information Division.
14. Gerlinger, P, Moebius, H, and Brueggmann, D (2001). An Implicit Multigrid Method for Turbulent Combustion. Journal of Computational Physics;167:247–276.
15. Spalart, P.R. and Allmaras, S.R. (1992). A One-Equation Turbulence Model for Aerodynamic Flows. AIAA Paper 92-0439.